electronics

MDPI

Article

Resonance Mechanism Analysis and Suppression of Grid-Connected Energy Storage Power Station Inverter

Weiheng Kuang [1], Jinchuan Guo [1], Lianhui Ning [2], Junyuan Zhang [2,*], Xinmei Gu [1], Sisi Chen [1], Shihong Shi [1], Weihan Hao [1], Min Zhou [1], Tiantian He [2] and Qingxin Wang [2]

[1] Guangdong Electric Power Design Institute, Ltd., Guangzhou 510663, China; kuangweihong@gedi.com.cn (W.K.); guojinchuan@gedi.com.cn (J.G.); guxinmei@gedi.com.cn (X.G.); chensisi@gedi.com.cn (S.C.); shishihong@gedi.com.cn (S.S.); haoweihan@gedi.com.cn (W.H.); zhoumin@gedi.com.cn (M.Z.)

[2] Department of Electrical Engineering, Xi'an Jiaotong University, Xi'an 710049, China; ninglh@xjtu.edu.cn (L.N.); tiantianhe@stu.xjtu.edu.cn (T.H.); wangqx888@stu.xjtu.edu.cn (Q.W.)

* Correspondence: 17396187615@stu.xjtu.edu.cn

Abstract

The increasingly prominent "double-high" characteristics (high penetration of renewable energy and high proportion of power electronic devices) in modern power systems pose severe challenges to secure and stable operation, especially due to wideband oscillations induced by grid-connected inverters. In view of the fact that existing impedance modeling for grid-forming control often neglects the decoupling effect of the LC filter capacitor and the dynamics of inner voltage/current loops, leading to inaccurate characterization of mid-to-high frequency impedance, this paper aims to establish more accurate impedance models for grid-connected inverters and to develop effective oscillation mitigation methods accordingly. First, the harmonic linearization method is adopted to derive refined positive- and negative-sequence impedance analytical models for NPC inverters under both grid-following and grid-forming control. Second, simulation-based frequency scanning is conducted to validate the accuracy of the proposed models, and the differences in system resonance characteristics under the two control modes are comparatively analyzed. Finally, oscillation suppression strategies based on active damping and virtual impedance are, respectively, designed. The results show that the proposed models can accurately characterize mid-to-high frequency impedance, reveal the distinct resonance mechanisms of different control modes, and the proposed suppression strategies can effectively attenuate wideband oscillations. These findings provide theoretical foundations and practical technical pathways for stability analysis and optimization design of inverter-grid systems in high-renewable-penetration scenarios.

Keywords: energy storage systems; grid-forming; grid-following; sequence impedance; stability analysis

Check for updates

Academic Editor: José Matas

Received: 23 April 2026
Revised: 10 May 2026
Accepted: 14 May 2026
Published: 21 May 2026

Copyright: © 2026 by the authors. Licensee MDPI, Basel, Switzerland. This article is an open access article distributed under the terms and conditions of the Creative Commons Attribution (CC BY) license.

1. Introduction

In recent years, clean energy sources such as wind and solar have grown rapidly, but their volatility and intermittency challenge grid stability and operation. The increasing penetration of renewable energy and power electronic devices leads to wideband oscillations, which pose a threat to the secure operation of energy storage systems connected to the grid [1,2].

The energy storage system employs a neutral-point clamped (NPC) three-level inverter as a power electronic component. Variations in power electronic topologies or control

strategies can alter the system's oscillation frequency, making stability analysis extremely challenging [3,4]. As the core equipment of the energy storage system, grid-connected inverters also face the challenge of broadband oscillations caused by impedance interaction.

For stability analysis, traditional methods include the state-space method [5] and the impedance analysis method [6]. The state-space method models system parameters based on dynamic equations and calculates eigenvalues and damping ratios, but it is computationally intensive. In contrast, the impedance analysis method treats the system as two independent subsystems at the interface, allowing the impedance matrix of only the affected subsystem to be reconstructed when changes occur, which significantly simplifies the analysis. So far, numerous stability studies have been conducted on photovoltaic power plants, which are similar to energy storage systems, and these provide important references for the stability analysis of energy storage systems. Reference [7] performed impedance modeling and stability analysis for grid-tied converters without phase-locked loop and voltage sensors, revealing alternative stability mechanisms. Reference [8] proposed a hybrid control strategy combining grid-following and grid-forming modes to enhance the stability of grid-connected inverters. Reference [9] employed a state-space method to perform small-signal modeling and stability analysis of parallel virtual synchronous generators. Some researchers have used harmonic linearization to establish VSG sequence impedance models [10], but these models typically neglect the LC filter capacitor branch and the dynamics of voltage-current inner loops.

In addition to the aforementioned studies on impedance modeling and VSG control, several recent works have addressed related aspects. For instance, ref. [11] characterized the impact of communication latencies on wide-synchronization control, revealing that delay-induced instabilities are sensitive to control asymmetries—an insight useful for designing robust damping controllers. Similarly, ref. [12] validated a DSP-controlled grid-tied inverter using CHIL simulation with RTDS, demonstrating that practical delays and discretization effects can be captured in impedance-based analysis, thereby supporting the engineering credibility of our active damping and virtual impedance strategies. From a theoretical perspective, ref. [13] proposed a manifold topology method to characterize the global stability domain of wind-power grid-connected systems, providing a novel way to quantify stability boundaries under large disturbances—a concept extendable to energy storage stations. Meanwhile, ref. [14] developed a neuro-adaptive fuzzy fractional-order super-twisting sliding mode control for PMSG-based WECS, achieving chattering-free, model-free MPPT. Although these works focus on wind energy conversion or time-delay analysis rather than directly on inverter resonance, their underlying ideas—adaptive chattering suppression, delay-robust feedback, and hardware-in-the-loop validation—complement the frequency-domain impedance approach of this paper and offer promising directions for future research.

In existing studies on Virtual Synchronous Generator (VSG) impedance modeling based on harmonic linearization, some models typically reduce the order of high-frequency dynamic components to simplify derivations or focus on low-frequency oscillation analysis. While this simplification results in minimal error when analyzing low- and medium-frequency band power oscillations, the model's accuracy significantly decreases when analyzing mid-to-high-frequency oscillations caused by the coupling between LCL/LC filter resonance peaks and inner-loop control, failing to accurately reflect the system's actual impedance crosspoints and phase margins. To reveal the broadband resonance risks that energy storage power stations may face, it is necessary to establish a grid-forming inverter sequence impedance model that balances computational efficiency with high-frequency accuracy. This paper addresses this need by establishing a comprehensive analytical sequence impedance model for grid-forming inverters that fully considers the LC filter capacitive branch and voltage-current inner-loop control.

To address the aforementioned shortcomings, this paper makes the following contributions: First, models of energy storage systems under grid-following and grid-forming control modes are established. Second, sequential impedance models of the energy storage systems under both control modes are developed; their validity is verified through sweep testing, and the differences in resonance behavior between the two control modes are compared. Based on this, an oscillation suppression strategy for grid-following control using active dampers and an oscillation suppression strategy for grid-forming control using virtual impedance are proposed.

2. Energy Storage System Topology and Simulation Modeling

At the equipment level, the grid-connection stability of energy storage power stations is primarily manifested in the interaction between their internal grid-connected inverters and grid impedance. Therefore, this paper focuses on the core power conversion equipment in energy storage power stations—the NPC-type three-level grid-connected inverter—and investigates its resonance mechanisms. The structure of the energy storage system is shown in Figure 1.

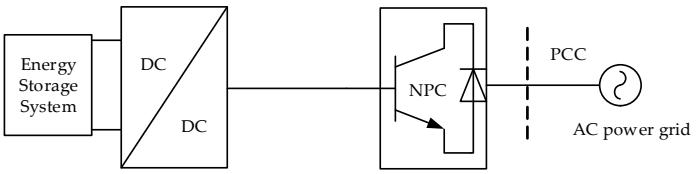


Figure 1. Energy storage system structure diagram.

The topology of the NPC converter is shown in Figure 2. This is a midpoint-clamped three-level converter topology. As shown in the figure, the control methods are divided into grid-following control and grid-forming control. Grid-following control is an inverter control strategy based on grid voltage synchronization, whose core principle is to use a phase-locked loop (PLL) to track the grid voltage, thereby synchronizing the NPC output voltage with the grid voltage. Grid-forming control employs Virtual Synchronous Generator (VSG) technology to simulate the autonomous voltage regulation capability of a synchronous generator via its excitation system, enabling the VSG to provide reactive power support similar to that of a conventional synchronous machine.

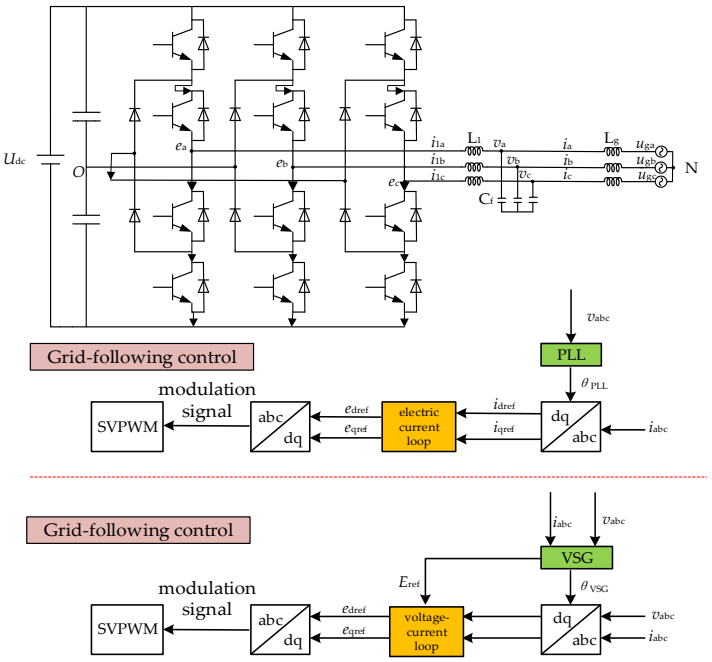


Figure 2. NPC Topology.

The state variables are the inductor current i_{1x} (x = a, b, c) on the inverter bridge side, the inductor current i_{2x} (x = a, b, c) on the grid-connected side, and the filter capacitor voltage v_x (x = a, b, c). The specific control procedures are shown in Appendix A.

Based on the energy storage system shown in Figure 1, grid-following and grid-forming PSCAD time-domain simulation models were developed. The specific simulation parameters are shown in Table 1. This is a model of a 1.75 MW energy storage system; the NPC converter parameters, grid-following control parameters, and grid-forming control parameters are listed in Table 1. The model parameters are derived from an energy storage project currently in the planning and construction phase. All subsequent simulation results in this paper are based on this model.

Table 1. Energy storage system parameters.

Equipment	Item	Parameter
NPC	Rated Capacity/MW	1.725
	DC-Side Voltage/kV	1.5
	AC-Side Line Voltage/kV	0.69
	DC-Side Capacitance/μF	2500
	Filter inductor/mH	0.5
	Filter capacitor/μF	500
grid-following	Reactive outer-loop control parameters	K_{p1} = 0.01, K_{i1} = 40
	Active outer-loop control parameters	K_{p2} = 14.2, K_{i2} = 0.22
	Phase-locked loop control parameters	K_{p3} = 0.01, K_{i3} = 40
	Current-loop control parameters	K_p = 900, K_i = 0.005
grid-forming	moment of inertia J	J = 0.2
	damping coefficient D	D = 150
	frequency modulation coefficient K_f	K_f = 30
	voltage regulation coefficient Kv	K_v = 1.5
	droop coefficient K_q	K_q = 0.0001
	Voltage loop control parameters	K_p = 8, K_i = 0.0303
	Current loop control parameters	K_p = 8, K_i = 0.00303

3. Sequence Impedance Modeling of Grid-Forming Inverter

3.1. Impedance Modeling of Grid-Following Converters

This section is based on the harmonic linearization method and draws on the basic framework for impedance modeling of grid-tied inverters presented in reference [7]; however, it further takes into account the dynamics of the LC filter capacitive branch in the NPC three-level topology.

The expressions for the midpoint voltage of the three-phase bridge arms, the voltage at the point of common connection (PCC), and the grid-connected current are as follows:

$$\begin{bmatrix} e_a \\ e_b \\ e_c \end{bmatrix} = sL \begin{bmatrix} i_a \\ i_b \\ i_c \end{bmatrix} + \begin{bmatrix} u_a \\ u_b \\ u_c \end{bmatrix} \tag{1}$$

where e_x(x = a, b, c) is the voltage at the converter output; i_x(x = a, b, c) is the current at the grid connection point; u_x(x = a, b, c) is the voltage at the converter's grid connection point; L is the filter inductance; s is the Laplace operator.

The expressions for the three-phase grid-connected currents i_a and v_a are:

$$\begin{aligned} i_a(t) &= I_1 \cos(2\pi f_1 t + \varphi_{i1}) + \\ & I_p \cos(2\pi f_p t + \varphi_{ip}) + I_n \cos(2\pi f_n t + \varphi_{in}) \end{aligned} \tag{2}$$

$$\begin{aligned} \mathrm{v}_a(t) &= V_1 \cos(2\pi f_1 t) + \\ & V_p \cos(2\pi f_p t + \varphi_{vp}) + V_n \cos(2\pi f_n t + \varphi_{vn}) \end{aligned} \tag{3}$$

where I_1, V_1 represent the fundamental current and fundamental voltage, respectively; f_1 represents the fundamental frequency; φ_{i1} is the phase of the fundamental current; V_{p}, V_{n}, I_{p} and I_{n} are the peak values of the positive- and negative-sequence voltage and current disturbances, respectively; f_{p}, and f_{n} are the frequencies of the positive- and negative-sequence disturbances, respectively; φ_{vp}, φ_{vn}, φ_{ip} and φ_{in} are the phases of the positive- and negative-sequence voltage and current disturbances, respectively.

In the frequency domain, the expression is:

$$\mathbf{V}_a[f] = \begin{cases} \mathbf{V}_1,\ f = \pm f_1 \\ \mathbf{V}_p,\ f = \pm f_p \\ \mathbf{V}_n,\ f = \pm f_n \end{cases} \tag{4}$$

$$\mathbf{I}_a[f] = \begin{cases} \mathbf{I}_1,\ f = \pm f_1 \\ \mathbf{I}_p,\ f = \pm f_p \\ \mathbf{I}_n,\ f = \pm f_n \end{cases} \tag{5}$$

where

$$\mathbf{V}_1 = V_1/2,\ \mathbf{V}_P = (V_P/2)e^{\pm j\varphi_{vp}},\ \mathbf{V}_n = (V_n/2)e^{\pm j\varphi_{vn}}$$
$$\mathbf{I}_1 = I_1/2,\ \mathbf{I}_P = (I_P/2)e^{\pm j\varphi_{ip}},\ \mathbf{I}_n = (I_n/2)e^{\pm j\varphi_{in}}$$

After performing a dq coordinate transformation on the voltage and current at the PCC point, The frequency-domain expressions for the PCC voltage considering PLL disturbances are:

$$\mathbf{I}_d[f] = \begin{cases} I_1 \cos\theta_i, \quad \mathrm{dc} \\ \mathbf{I}_p,\ f = \pm(f_p - f_1) \\ \mathbf{I}_n,\ f = \pm(f_n + f_1) \end{cases} \tag{6}$$

$$\mathbf{I}_q[f] = \begin{cases} I_1 \sin\theta_i, \quad \mathrm{dc} \\ \mp j\mathbf{I}_p,\ f = \pm(f_p - f_1) \\ \pm j\mathbf{I}_n,\ f = \pm(f_n + f_1) \end{cases} \tag{7}$$

where ($\mathrm{f_p} - \mathrm{f_1}$) represents the frequency of the small-signal component in the d-q coordinate system after a frequency shift resulting from the transformation of the positive-sequence three-phase disturbance into the *d-q* domain via the Park coordinate transformation; ($\mathrm{f_n} + \mathrm{f_1}$) represents the frequency of the small-signal component in the *d-q* coordinate system after a frequency shift resulting from the transformation of the negative-sequence three-phase disturbance into the *d-q* domain via the Park coordinate transformation.

$$\mathbf{V}_{d1}[f] = \begin{cases} V_1, \quad \mathrm{dc} \\ \mathbf{V}_p,\ f = \pm(f_p - f_1) \\ \mathbf{V}_n,\ f = \pm(f_n + f_1) \end{cases} \tag{8}$$

$$\mathbf{V}_{q1}[f] = \begin{cases} 0, \quad \mathrm{dc} \\ \mp j\mathbf{V}_p,\ f = \pm(f_p - f_1) \\ \pm j\mathbf{V}_n,\ f = \pm(f_n + f_1) \end{cases} \tag{9}$$

Frequency-domain expression for the voltage at the grid connection point, taking into account disturbances in the phase-locked loop:

$$\mathbf{V}_d[f] = \begin{cases} V_1, \quad \mathrm{dc} \\ \mathbf{V}_p,\ f = \pm(f_p - f_1) \\ \mathbf{V}_n,\ f = \pm(f_n + f_1) \end{cases} \tag{10}$$

$$\mathbf{V}_q[f] = \begin{cases} 0, \quad \text{dc} \\ [-G_p(s)V_1 \mp j]\mathbf{V}_p, \\ f = \pm(f_p - f_1) \\ [-G_n(s)V_1 \pm j]\mathbf{V}_n, \\ f = \pm(f_n + f_1) \end{cases} \tag{11}$$

As shown in the synchronous phase-locked loop in Appendix A, the transfer function between small-signal voltage disturbances and $\Delta\theta$ is given by:

$$\Delta\boldsymbol{\theta}[f] = \begin{cases} G_p(s)\mathbf{V}_p, \ f = \pm(f_p - f_1) \\ G_n(s)\mathbf{V}_n, \ f = \pm(f_n + f_1) \end{cases} \tag{12}$$

The transfer function expressions for the positive- and negative-sequence are as follows:

$$G_p(s) = \mp jH_{pll}(s)/[1 + V_1H_{pll}(s)] \tag{13}$$

$$G_n(s) = \pm jH_{pll}(s)/[1 + V_1H_{pll}(s)] \tag{14}$$

where $H_{pll}(s) = (k_{p-pll} + k_{i-pll}/s)/s$ represents the PI parameters of the phase-locked loop; $G_p(s)$ is the forward transfer function; $G_n(s)$ is the reverse transfer function.

From Equation (12), we obtain:

$$\sin\theta_{pll}[f] = \begin{cases} \mp\frac{j}{2}, \quad f = f_1 \\ \mp j\frac{1}{2}\frac{T_{pll}(s\mp 2\pi f_1)}{V_1}\mathbf{V}_p, \\ f = f_p \\ \pm j\frac{1}{2}\frac{T_{pll}(s\mp 2\pi f_1)}{V_1}\mathbf{V}_n, \\ f = f_n \end{cases} \tag{15}$$

$$\cos\theta_{pll}[f] = \begin{cases} \frac{1}{2}, \ f = f_1 \\ \frac{1}{2}\frac{T_{pll}(s\mp 2\pi f_1)}{V_1}\mathbf{V}_p, \\ f = f_p \\ \frac{1}{2}\frac{T_{pll}(s\pm 2\pi f_1)}{V_1}\mathbf{V}_n, \\ f = f_n \end{cases} \tag{16}$$

Disturbance current considering the PLL effect:

$$\mathbf{I}_d[f] = \begin{cases} I_1\cos\theta_i, \quad \text{dc} \\ \mp jI_1\sin\theta_i\frac{T_{pll}(s)}{V_1}\mathbf{V}_p + \mathbf{I}_p, \\ f = \pm(f_p - f_1) \\ \mp jI_1\sin\theta_i\frac{T_{pll}(s)}{V_1}\mathbf{V}_n + \mathbf{I}_n, \\ f = \pm(f_n + f_1) \end{cases} \tag{17}$$

$$\mathbf{I}_q[f] = \begin{cases} I_1\sin\theta_i, \quad \text{dc} \\ \mp jI_1\cos\theta_i\frac{T_{pll}(s)}{V_1}\mathbf{V}_p \mp j\mathbf{I}_p, \\ f = \pm(f_p - f_1) \\ \mp jI_1\sin\theta_i\frac{T_{pll}(s)}{V_1}\mathbf{V}_n \pm j\mathbf{I}_n, \\ f = \pm(f_n + f_1) \end{cases} \tag{18}$$

Substituting into the current control loop and applying the inverse Park transformation yields the final positive- and negative-sequence impedances as:

$$\mathbf{Z_p}(s) = \frac{sL+H(s-2\pi f_1)-j\omega L}{-\frac{1}{2}j\frac{T_{pll}(s-2\pi f)}{V_1}H(s-2\pi f_1)(I_{dref}+jI_{qref})} \tag{19}$$

$$\mathbf{Z_n}(s) = \frac{sL+H(s+2\pi f_1)+j\omega L}{-\frac{1}{2}j\frac{T_{pll}(s+2\pi f)}{V_1}H(s+2\pi f_1)(I_{dref}-jI_{qref})} \tag{20}$$

3.2. Impedance Modeling of Grid-Forming Converters

Unlike the VSG impedance models established in [10,11], this section preserves the full dynamics of the LC filter capacitance branch and the voltage-current inner loop during the modeling process, rather than simplifying them, thereby improving the model's accuracy in the mid-to-high frequency range.

Grid-forming control is centered around a virtual synchronous generator (VSG). The grid-forming NPC employs an LC second-order circuit, and the relationship between the midpoint voltage of its three-phase bridge arms and the voltage and current at the point of common connection (PCC) is expressed as follows:

$$\begin{bmatrix} e_a \\ e_b \\ e_c \end{bmatrix} = (sL_f)\begin{bmatrix} i_a \\ i_b \\ i_c \end{bmatrix} + (s^2L_fC_f+1)\begin{bmatrix} u_a \\ u_b \\ u_c \end{bmatrix} \tag{21}$$

The phase angle expression derived from the mathematical equation for the active component is:

$$\theta = M(s)(\omega_n D_p + \frac{P_{set}}{\omega_n} - \frac{P_e}{\omega_n}) \tag{22}$$

where $M(s) = 1/(js^2 + D_p s)$; w_n is the rated angular frequency; D_p is the damping coefficient; P_{set} is the power setpoint; P_e is the rated power;

In the phase angle expression, we primarily consider the linear terms and neglect the small quadratic nonlinear terms, resulting in:

$$\theta[f] = \begin{cases} 1.5[V_1 I_1 \cos\varphi_{i1} + V_p I_p \cos(\varphi_{vp} - \varphi_{ip}) \\ +V_n I_n \cos(\varphi_{vn} - \varphi_{in})], \text{ dc} \\ \frac{-M(s)}{\omega_n} \cdot 3(\mathbf{V_1}^*\mathbf{I}_p + \mathbf{V_p}^*\mathbf{I_1}),\ f = \pm(f_p - f_1) \\ \frac{-M(s)}{\omega_n} \cdot 3(\mathbf{V_1 I_n} + \mathbf{V_n I_1}),\ f = \pm(f_p - f_1) \end{cases} \tag{23}$$

The phase angles of the grid-forming inverter output, after being subjected to positive-sequence and negative-sequence disturbances, are divided into two components: θ represents the phase angle output of the inverter without disturbances, while $\Delta\theta$ represents the phase angle disturbance caused by the introduction of a small harmonic disturbance signal. The frequency-domain expression is as follows:

$$\Delta\theta[f] = \begin{cases} \frac{-M(s)}{\omega_n} \cdot 3(\mathbf{V_1}^*\mathbf{I}_p + \mathbf{V_p}^*\mathbf{I_1}),\ f = \pm(f_p - f_1) \\ \frac{-M(s)}{\omega_n} \cdot 3(\mathbf{V_1 I_n} + \mathbf{V_n I_1}),\ f = \pm(f_n - f_1) \end{cases} \tag{24}$$

Linearize $\cos\theta$ and $\sin\theta$:

$$\cos\theta = \cos(\theta_1 + \Delta\theta) \approx \cos\theta_1 - \Delta\theta\sin\theta_1 \tag{25}$$

$$\sin\theta = \sin(\theta_1 + \Delta\theta) \approx \sin\theta_1 + \Delta\theta\cos\theta_1 \tag{26}$$

where θ_1 represents the phase angle output value in the absence of interference.

By transforming the cosine and sine functions into the frequency domain, applying the frequency-domain convolution theorem, and neglecting the nonlinear coupling terms, we obtain the following frequency-domain expression:

$$\cos\theta_{pll}[f] = \begin{cases} \frac{1}{2},\ f = \pm f_1 \\ \mp j\frac{M(s\mp j2\pi f_1)}{2\omega_n}\cdot \\ 3(\mathbf{V_1}^*\mathbf{I_p} + \mathbf{V_p}^*\mathbf{I_1}),\ f = \pm f_p \\ \pm j\frac{M(s\mp j2\pi f_1)}{2\omega_n}\cdot \\ 3(\mathbf{V_1}\mathbf{I_n} + \mathbf{V_n}\mathbf{I_1}),\ f = \pm f_n \end{cases} \tag{27}$$

$$\sin\theta_{pll}[f] = \begin{cases} \mp\frac{j}{2},\quad f = \pm f_1 \\ \frac{-M(s\mp j2\pi f_1)}{2\omega_n}\cdot \\ 3(\mathbf{V_1}^*\mathbf{I}_p + \mathbf{V_p}^*\mathbf{I_1}),\ f = \pm f_p \\ \frac{-M(s\mp j2\pi f_1)}{2\omega_n}\cdot \\ 3(\mathbf{V_1}\mathbf{I_n} + \mathbf{V_n}\mathbf{I_1}),\ f = \pm f_n \end{cases} \tag{28}$$

The positive- and negative-sequence decompositions of the various components of the control loop, and their expressions in the frequency domain, are as follows:

$$v_d[f] = \begin{cases} V_1,\ \mathrm{dc} \\ \mathbf{V_p},\ f = \pm(f_p - f_1) \\ \mathbf{V_n},\ f = \pm(f_p - f_1) \end{cases} \tag{29}$$

$$v_q[f] = \begin{cases} 0,\ \mathrm{dc} \\ \mp j\mathbf{V_p},\ f = \pm(f_p - f_1) \\ \pm j\mathbf{V_n},\ f = \pm(f_p - f_1) \end{cases} \tag{30}$$

$$i_q[f] = \begin{cases} I_1\sin\theta_{i1},\ \mathrm{dc} \\ \mp j\mathbf{I_p},\ f = \pm(f_p - f_1) \\ \pm j\mathbf{I_n},\ f = \pm(f_p - f_1) \end{cases} \tag{31}$$

$$i_{ld}[f] = \begin{cases} I_1\cos\theta_{i1} + sC_f\cdot V_1,\ \mathrm{dc} \\ \mathbf{I_p} + sC_f\cdot\mathbf{V_p},\ f = \pm(f_p - f_1) \\ \mathbf{I_n} + sC_f\cdot\mathbf{V_n},\ f = \pm(f_p - f_1) \end{cases} \tag{32}$$

$$i_{lq}[f] = \begin{cases} I_1\sin\theta_{i1},\ \mathrm{dc} \\ \mp j\mathbf{I_p} \mp jsC_f\cdot\mathbf{V_p},\ f = \pm(f_p - f_1) \\ \pm j\mathbf{I_n} \pm jsC_f\cdot\mathbf{V_n},\ f = \pm(f_p - f_1) \end{cases} \tag{33}$$

Substitute into the voltage-current control loop, then apply the inverse Park transformation to the main circuit equations to obtain the final expression:

$$Z_p(s) = \frac{R_f + sL_f + K\cdot U_{dc}\cdot(\mathbf{V_1^*}\cdot M_p + G_i(s))}{1 + sC_f(R_f + sL_f) + K\cdot U_{dc}\cdot(\mathbf{I_1^*}\cdot M_p + G_i(s)(G_v(s)) + sC_f)} \tag{34}$$

$$Z_n(s) = \frac{R_f + sL_f + K\cdot U_{dc}\cdot(\mathbf{V_1^*}\cdot M_n + G_i(s))}{1 + sC_f(R_f + sL_f) + K\cdot U_{dc}\cdot(\mathbf{I_1^*}\cdot M_n + G_i(s)(G_v(s)) + sC_f)} \tag{35}$$

3.3. Sweep Verification

A disturbance signal is injected into a specific grid connection point, and the corresponding current signal at that point is acquired. The voltage and current signals are then processed and calculated to solve for the system's sequence impedance model.

The resulting grid-following and grid-forming sequence impedance models are shown in Figures 3 and 4.

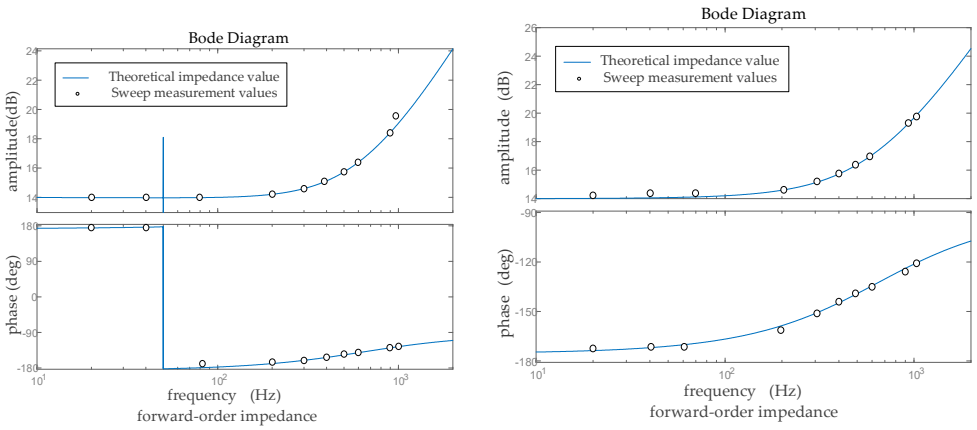


Figure 3. Impedance model of grid-following system.

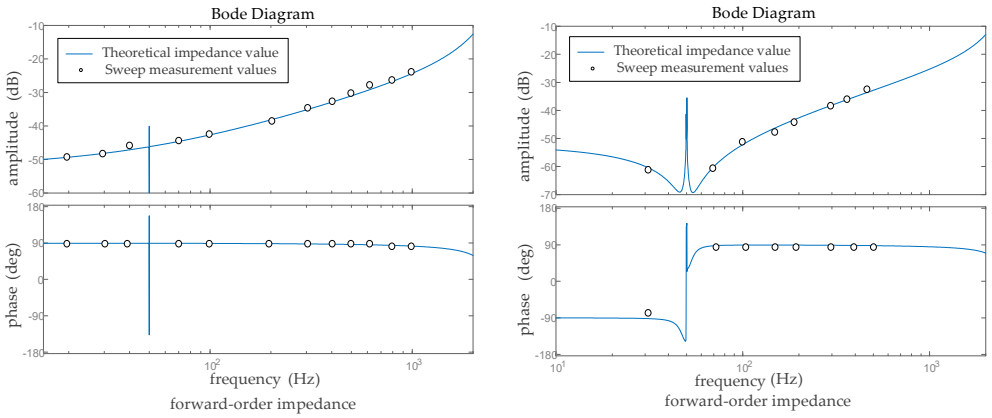


Figure 4. Impedance model of grid-forming system.

The magnitude of the sequence impedance model established for grid-forming energy storage systems is significantly smaller than that of the impedance model established for grid-following energy storage systems. The sequence impedance established for grid-following energy storage systems exhibits a capacitive, or negative, impedance characteristic. When the impedance phase angle is less than -90° and intersects with the grid impedance magnitude, the phase margin at the intersection point is insufficient, making it prone to interaction with the inductive grid and potentially triggering related oscillation issues. The positive-sequence impedance of a grid-forming energy storage system is essentially inductive in the medium-to-high frequency range. In the low-frequency range, the positive-sequence impedance of a grid-forming system exhibits capacitive characteristics due to the influence of the capacitor in the LC filter; however, since its phase angle is greater than -90°, it will not cause oscillation or instability when connected to an inductive grid. The negative-sequence impedance of a grid-forming energy storage system remains inductive throughout. However, around 50 Hz, both the magnitude and phase of the sequence impedance exhibit significant fluctuations. In grid-forming systems, the phase angle of the sequence impedance model is less than -90°. When the phase margin at the intersection point is insufficient, this can easily lead to system oscillation and instability; therefore,

grid-forming systems are prone to oscillations around 50 Hz, known as sub-synchronous oscillations. The differences in resonance between these two control models are primarily due to variations in the grid type and grid-forming control loops, which result in different impedance characteristics. It should be noted that existing literature primarily focuses on low-frequency oscillation modes dominated by the VSG power loop, which are mainly generated by the interaction between the virtual inertia of the active power loop and the grid impedance. The "prone to oscillation around 50 Hz" phenomenon identified in this paper refers to sub-synchronous oscillation modes near the fundamental frequency.

4. Oscillation Suppression Strategy

4.1. A Grid-Following Oscillation Suppression Strategy Based on Active Dampers

For grid-following systems, to ensure the system operates in a stable state, a certain level of system damping must be provided to address specific operating conditions that could lead to oscillation and instability. System damping is determined by the main circuit parameters, the steady-state operating point, and the control parameters. The use of an active damping controller is an effective method for suppressing system oscillations. Essentially, this involves reshaping the system's impedance to ultimately identify a suitable active damping controller. There are generally two approaches to impedance reshaping: first, ensuring that the amplitude-frequency curves of the grid impedance and the equivalent impedance of the grid-following system never intersect under specific operating conditions; second, ensuring that when the grid impedance and the equivalent impedance of the grid-following system do intersect under specific operating conditions, the phase margin at that phase difference is less than 180°. The active damping controller designed in this paper is shown in Figure 5. Figure 6 shows a flowchart of an oscillation suppression strategy for a grid-following energy storage system based on an active damping controller.

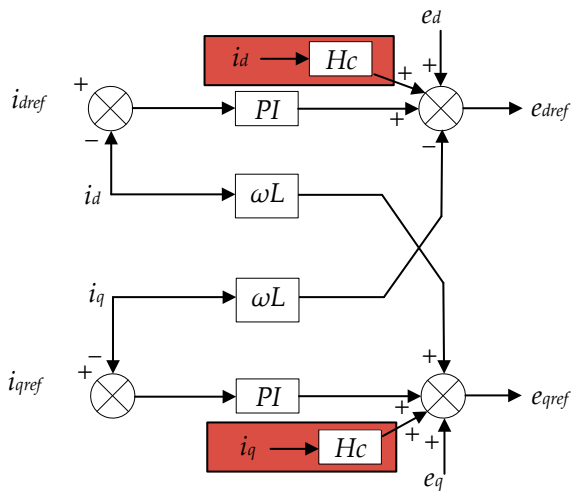


Figure 5. Block diagram of current inner-loop control for an impedance-reconfigured grid-following System.

After adding the active damping controller, the current-loop controller for the grid-connected energy storage system becomes:

$$\begin{cases} e_d = (I_{dref} - i_d)H(s) - \omega L \cdot i_q + v_d + H_c(s)i_d \\ e_q = (I_{qref} - i_d)H(s) - \omega L \cdot i_d + v_q + H_c(s)i_q \end{cases} \tag{36}$$

$$H_c(s) = \frac{k_r s}{s + \omega_c} \tag{37}$$

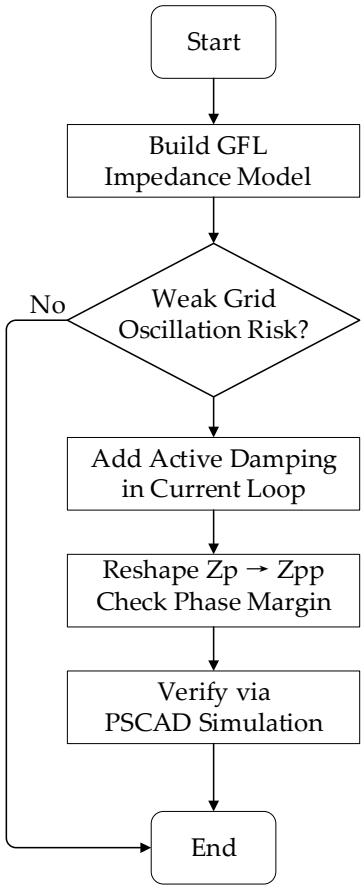


Figure 6. Flowchart of an oscillation suppression strategy for a grid-following energy storage system based on an active damping controller.

The reshaped positive and negative sequence impedances are:

$$\mathbf{Z_p}(s) = \frac{sL + H(s - 2\pi f_1) - j\omega L - H_c(s - 2\pi f_1)}{-\frac{1}{2}j\frac{T_{pll}(s-2\pi f)}{V_1}H(s - 2\pi f_1)(I_{dref} + jI_{qref})} \tag{38}$$

$$\mathbf{Z_n}(s) = \frac{sL + H(s + 2\pi f_1) + j\omega L - H_c(s + 2\pi f_1)}{-\frac{1}{2}j\frac{T_{pll}(s+2\pi f)}{V_1}H(s + 2\pi f_1)(I_{dref} - jI_{qref})} \tag{39}$$

Assume that the system is in an oscillatory unstable state without a damping controller. The system impedance curve is Zp, and the grid-side impedance curve is Zg. Let kr = 5 and w = 200 rad/s. After adding a damping controller, the reshaped impedance curve is Zpp. Its positive-sequence Bode plot is shown below:

As shown in Figure 7, without a damping controller, when the system impedance is equal in magnitude to the grid impedance, the phase difference is 251°, resulting in insufficient phase margin. With the damping controller, the phase difference is −70°, which is less than 180°, ensuring a positive phase margin and maintaining system stability. Unlike conventional active damping designs, this paper addresses the capacitive negative damping characteristics exhibited by grid-following energy storage inverters in weak grid conditions. By connecting a bandpass filter in parallel at the current inner-loop command, the phase at the intersection with the grid impedance is precisely reshaped. This method employs parameter tuning based on the exact impedance model derived earlier (such as the selection of Kr and ω in Equation (38)), achieving robustness against variations in grid impedance.

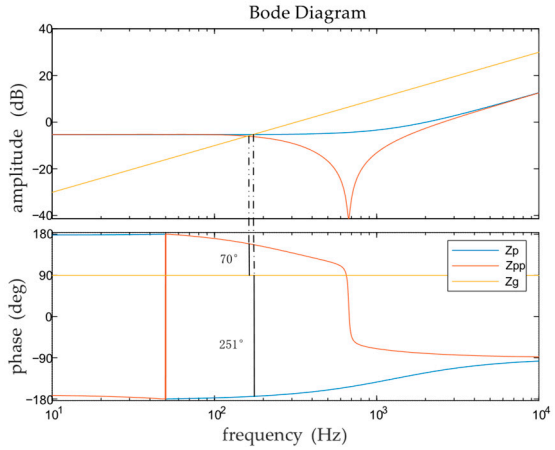


Figure 7. Bode diagram of impedance curve without a damping controller and with a damping controller.

4.2. Grid-Following System Simulation and Verification

Under the default parameter settings, when t = 2 s is set in the PSCAD/EMTDC platform, and the grid-side impedance is 6 p.u. of its original value, the oscillation waveform is shown in Figure 8 (SCR = 1.425 under weak grid conditions). Under the default parameter settings, when t = 2 s is set in the PSCAD/EMTDC platform, the grid-side impedance is 6 p.u. of its original value, and the damping controller is engaged, the three-phase output current waveforms are shown in Figure 9. Before the damping controller was applied, the system current exhibited a divergent oscillation trend; after the damping controller was applied, the system current remained stable. This demonstrates that the active damping controller designed in this paper for grid-following systems can effectively suppress system oscillations.

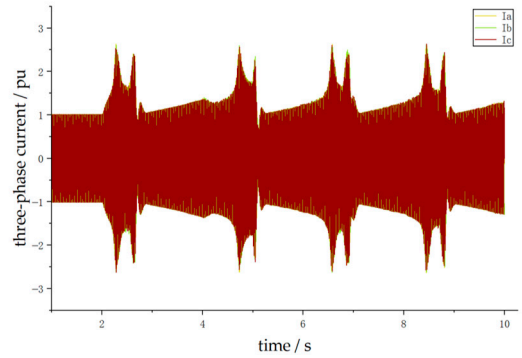


Figure 8. Current waveform without active damping controller.

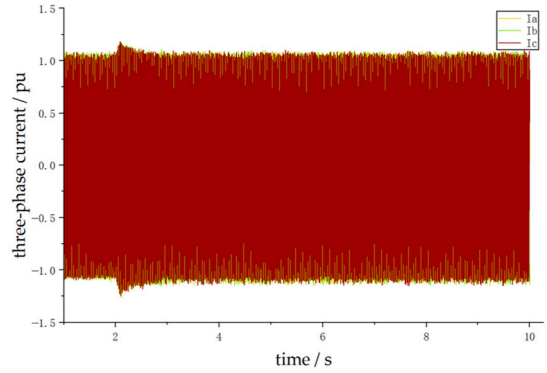


Figure 9. Current waveform of the grid-following system before and after the active damping controller is put into operation.

4.3. A Grid-Forming Oscillation Suppression Strategy Based on Virtual Impedance

In a strong grid scenario, to improve the stability of a Virtual Synchronous Generator (VSG) grid-forming system, the VSG's output impedance must be adjusted to avoid the frequency range where harmonic oscillations are induced by insufficient phase margin during interaction with the grid impedance. To achieve this, virtual impedance control can be introduced after the VSG's reactive power control stage. By adding a current feedback loop, the voltage drop across the virtual impedance, generated by the output current, is used to correct the voltage reference, thereby regulating the VSG's output impedance. Figure 10 shows the control block diagram of the grid-connected energy storage system with virtual impedance. Figure 11 shows a flowchart of an oscillation suppression strategy for grid-forming energy storage systems based on virtual impedance.

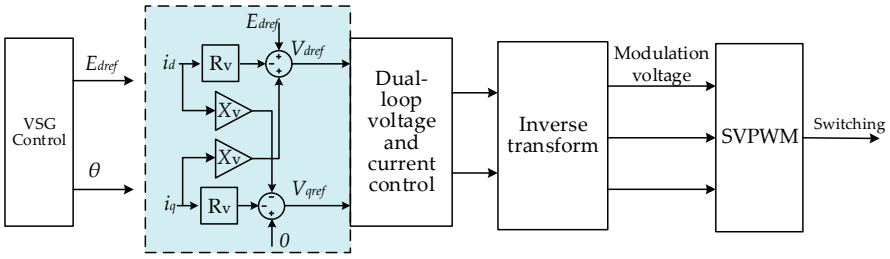


Figure 10. Control block diagram with virtual impedance.

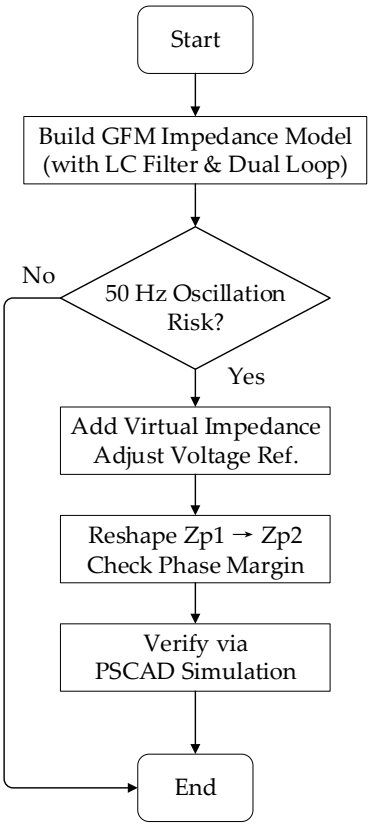


Figure 11. Flowchart of an oscillation suppression strategy for grid-connected energy storage systems based on virtual impedance.

The expression is as follows:

$$\begin{cases} V_{dref} = E_{dref} - R_v i_d + \omega L_v i_q \\ V_{qref} = 0 - R_v i_q - \omega L_v i_d \end{cases} \quad (40)$$

The reshaped positive and negative sequence impedances are:

$$\mathbf{Z_p}(s) = \frac{sL + H(s - 2\pi f_1) - j\omega L - H_c(s - 2\pi f_1)}{-\frac{1}{2}j\frac{T_{pll}(s-2\pi f)}{V_1}H(s - 2\pi f_1)(I_{dref} + jI_{qref})} \tag{41}$$

$$\mathbf{Z_n}(s) = \frac{sL + H(s + 2\pi f_1) + j\omega L - H_c(s + 2\pi f_1)}{-\frac{1}{2}j\frac{T_{pll}(s+2\pi f)}{V_1}H(s + 2\pi f_1)(I_{dref} - jI_{qref})} \tag{42}$$

Assume that the system is in an oscillatory and unstable state without a damping controller. The system impedance curve is Zp1, and the grid-side impedance curve is Zg. Let the inductance of the virtual impedance be equal to the filter inductance. After applying virtual impedance control, the reshaped impedance curve is Zp2, and its Bode plot is shown below:

Without the virtual impedance, the impedance is capacitive in the low-frequency range. Although instability does not occur, the stability margin is small, and the amplitude and phase angle fluctuate significantly near 50 Hz. At this frequency, the phase margin is insufficient, making the system prone to sub-synchronous oscillations. After introducing the damping controller, the impedance becomes inductive in the low-frequency range, increasing the stability margin. Furthermore, phase angle fluctuations near 50 Hz are minimal, the phase difference with the grid impedance is less than 180°, and the phase margin is greater than 0, ensuring the system remains stable.

To address the risk of sub-synchronous resonance near 50 Hz in grid-forming systems, this paper proposes introducing a virtual impedance equivalent to the filter inductance. The distinctive feature of this strategy is that its design objective is not to improve the low-frequency stability of the power loop, but rather to offset the phase lag caused by the capacitive region of the filter by adjusting the inductive component of the virtual impedance, thereby smoothing out fluctuations in the phase-frequency curve near 50 Hz. Simulation results (Figure 12) indicate that this method specifically addresses mid-to-high-frequency resonances caused by interactions between the inner loop and the filter, complementing conventional strategies that rely on increasing inertia to suppress low-frequency oscillations.

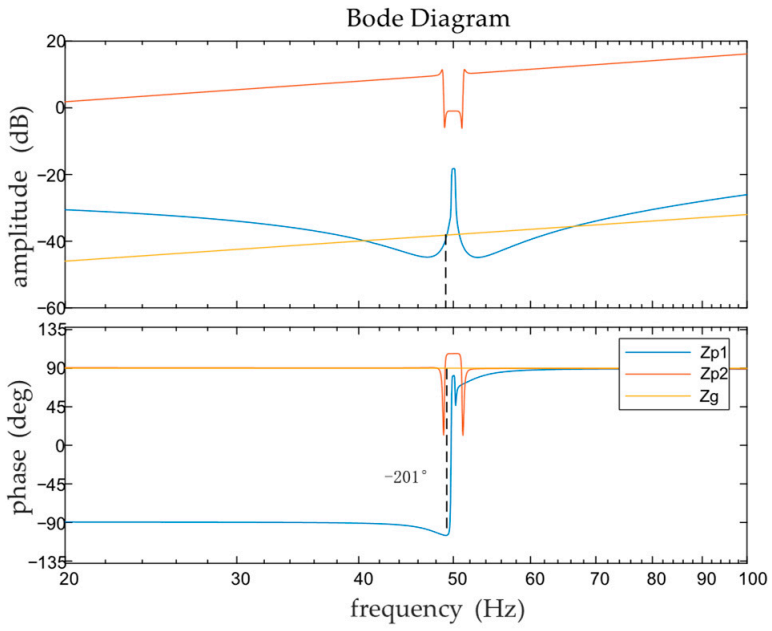


Figure 12. Bode diagram of impedance curve without virtual impedance controller and with virtual impedance controller.

4.4. Grid-Forming System Simulation and Verification

Under the default parameter settings, the grid impedance was set to 0.4 p.u. in the PSCAD/EMTDC platform and applied at t = 8 s (SCR = 5.35 under strong grid conditions). The three-phase current waveforms and active power oscillation waveforms are shown in Figures 13 and 14. Under the default parameter settings, when the grid-side impedance is set to 6 p.u. at t = 8 s on the PSCAD/EMTDC platform, and a virtual impedance controller is engaged, the three-phase current waveforms and active power waveforms are shown in Figures 15 and 16.

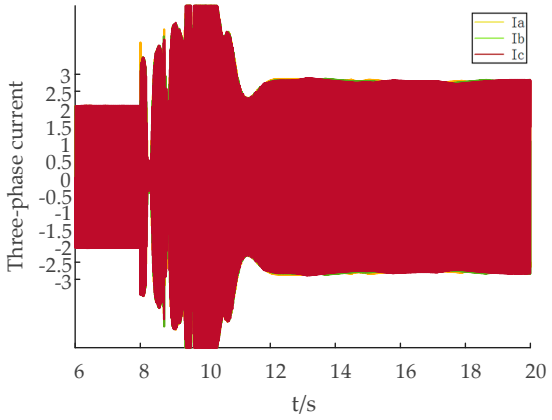


Figure 13. Three-phase current waveform without a virtual impedance controller.

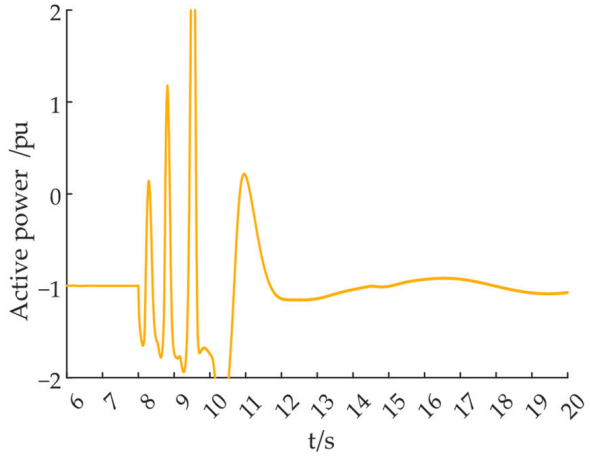


Figure 14. Active power waveform without adding a virtual impedance controller.

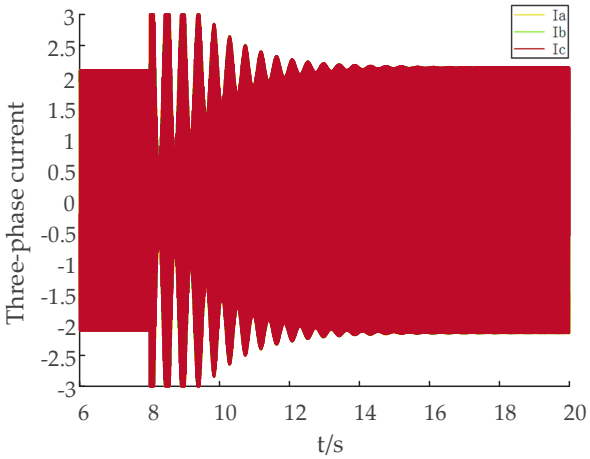


Figure 15. Three-phase current waveform with virtual impedance controller.

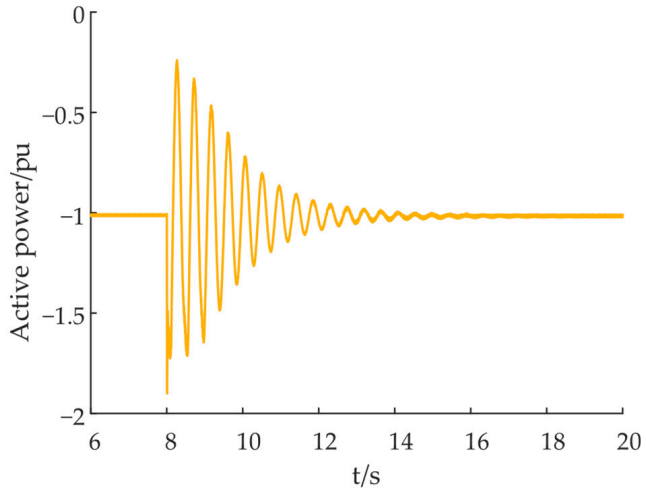


Figure 16. Active power waveform with virtual impedance controller.

Before the virtual impedance controller was added, the system current exhibited an oscillatory trend; as shown in Figures 15 and 16, after the virtual impedance controller was activated, the system current and power remained stable. These results demonstrate that the virtual impedance controller designed in this paper, based on a grid-forming system, can effectively suppress system oscillations.

4.5. Practical Implementation Challenges of the Proposed Strategies

In practical energy storage power stations, implementing the proposed active damping and virtual impedance strategies faces several non-ideal factors: time delays from sampling, PWM update, and anti-aliasing filters [15,16] can erode the phase margin of the active damping controller; temperature-induced drift of filter inductor/capacitor values (e.g., the 0.5 mH and 500 μF in Table 1) shifts the LC resonance frequency and may degrade robustness; in multi-inverter parallel configurations, uncoordinated virtual impedance settings can cause circulating currents and impair reactive power sharing; measurement noise and limited sensor resolution challenge the extraction of weak resonant components, especially when using small-amplitude disturbance injection; and the additional computational burden of band-pass filters (active damping) and extra feedback loops (virtual impedance) must be accommodated within real-time control hardware. These engineering challenges can be alleviated through phase-lead compensation, online impedance identification [17], droop-based coordination among parallel units [18,19], multi-sine injection with synchronous demodulation, and low-order filter approximations, respectively [20].

5. Conclusions

This paper focuses on grid-following and grid-forming energy storage inverters. Using a harmonic linearization method, wide-band sequence impedance modeling is performed. Combined with simulation verification, the resonance mechanisms under different control modes are revealed, and targeted oscillation suppression strategies are ultimately proposed. The main conclusions are as follows:

(1) Using the harmonic linearization method, a sequence impedance model for a grid-following energy storage inverter—including a phase-locked loop (PLL) control loop and an inner current control loop—was derived. Additionally, a detailed main circuit model incorporating filter capacitance was established, along with a sequence impedance model for a grid-forming energy storage inverter that encompasses capacitive feedback, inductive feedback, and dual-loop voltage-current control.

(2) The sequence impedance of grid-following energy storage systems exhibits capacitive characteristics across most frequency bands, making them prone to coupled oscillations with inductive power grids. In contrast, the positive-sequence impedance of grid-forming energy storage systems is predominantly inductive in the medium-to-high frequency bands, ensuring better stability when connected to inductive power grids. However, near 50 Hz, its magnitude-frequency characteristics fluctuate significantly, making it susceptible to sub-synchronous oscillations.

(3) For grid-following systems, this paper proposes an oscillation suppression method based on an active damping controller and reformulates the sequence impedance model derived earlier; for grid-forming systems, an oscillation suppression strategy based on virtual impedance control is further proposed, and a sequence impedance model of a virtual synchronous generator (VSG) incorporating virtual impedance control is established. Subsequently, through comparative analysis using Bode plots, the interaction characteristics between the sequence impedance and the grid impedance before and after the introduction of the controller were investigated. Furthermore, the correctness and effectiveness of the oscillation suppression strategies proposed in this paper for both grid-following and grid-forming energy storage systems were verified through time-domain simulations on the PSCAD/EMTDC simulation platform.

Author Contributions: Conceptualization, W.K. and L.N.; methodology, L.N., J.Z., T.H. and Q.W.; software, J.Z.; formal analysis, J.G. and X.G.; investigation, S.C. and S.S.; resources, J.Z.; data curation, J.Z.; writing—original draft preparation, J.Z. and Q.W.; writing—review and editing, L.N., J.G. and W.K.; visualization, W.H., M.Z. and T.H.; supervision, L.N.; project administration, L.N. All authors have read and agreed to the published version of the manuscript.

Funding: This research was funded by the National Key Research and Development Program of China, grant number 2021YFB3800200, and the Science and Technology Project of China Energy Engineering Group Guangdong Electric Power Design Institute Co., Ltd., grant number EV11001W. The APC was funded by China Energy Engineering Group Guangdong Electric Power Design Institute Co., Ltd.

Data Availability Statement: The data used are confidential.

Conflicts of Interest: Authors Weiheng Kuang, Jinchuan Guo, Xinmei Gu, Sisi Chen, Shihong Shi, Weihan Hao and Min Zhou were employed by Guangdong Electric Power Design Institute, Ltd., Guangzhou, Chine. The remaining authors declare that the research was conducted in the absence of any commercial or financial relationships that could be construed as a potential conflict of interest. The authors declare that this study received funding from China Energy Engineering Group Guangdong Electric Power Design Institute Co., Ltd. The funder was not involved in the study design, collection, analysis, interpretation of data, the writing of this article or the decision to submit it for publication.

Abbreviations

The following abbreviations are used in this manuscript:

NPC	Neutral Point Clamped
VSG	Virtual Synchronous Generator
PCC	Point of Common Coupling
PLL	Phase Locked Loop

Appendix A

There are many types of phase-locked loops (PLLs) used in network-based control systems. This paper models a PLL in a synchronous reference coordinate system; its block diagram is shown in Figure A1. In the figure, Kp_pll and Ki_pll represent the proportional and integral coefficients of the PLL's PI control, respectively.

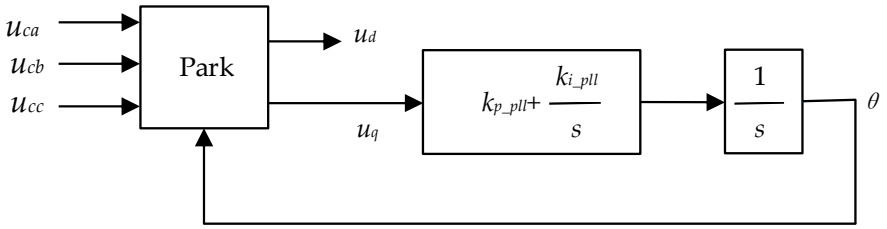


Figure A1. Flowchart of a Synchronous Reference Frame PLL.

The inner loop design for the mesh current is as follows:

$$\begin{cases} e_{dref} = u_d + (K_{p_I} + K_{i_I}/s)(i_{\text{dref}} - i_d) - \omega L_f \cdot i_q \\ e_{qref} = u_q + (K_{p_I} + K_{i_I}/s)(i_{\text{qref}} - i_q) + \omega L_f \cdot i_d \end{cases} \tag{A1}$$

where i_{dref} and i_{qref} are the reference commands for the d-axis and q-axis inductance currents, respectively, in the synchronous rotating coordinate system; u_d and u_q are the voltages at the PCC points on the d-axis and q-axis, respectively, in the synchronous rotating coordinate system; K_{p_I} and K_{i_I} are the proportional and integral coefficients of the current inner-loop PI control.

The grid-coupled outer-loop control employs virtual synchronous machine control, utilizing a second-order model of a synchronous generator to simulate the mechanical characteristics of a virtual synchronous machine.

$$\begin{cases} \frac{d\theta}{dt} = \omega \\ j\frac{d\omega}{dt} = T_m - T_e - D(\omega - \omega_0) \end{cases} \tag{A2}$$

To simulate the governor of a synchronous generator, its active power reference Pm can be expressed as:

$$P_m = P_{ref} + K_f(\omega_0 - \omega) \tag{A3}$$

where P_{ref} is the power reference value, and K_f is the primary frequency modulation coefficient.

The block diagram of the active power control loop is as follows:

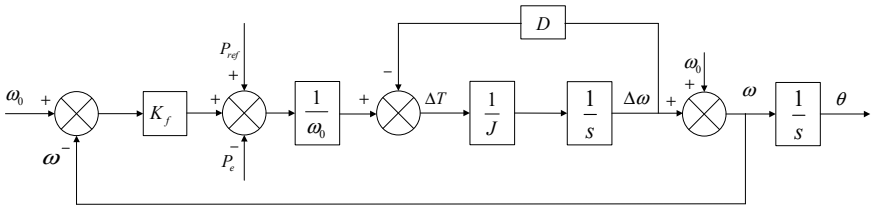


Figure A2. Active Power Control Block Diagram.

The relationship between reactive power deviation and the virtual potential E is as follows:

$$E = U_n + K_Q \int (Q_m - Q_e)dt \tag{A4}$$

where E is the magnitude of the virtual potential, K_Q is the integration coefficient, Q_m is the reactive power command, and Q_e is the output reactive power.

The reactive power command Qm is given by:

$$Q_m = Q_{ref} + K_v(U_n - U_0) \tag{A5}$$

where Q_{ref} is the setpoint for reactive power, K_V is the reactive power droop coefficient, U_n is the rated voltage amplitude, and U_0 is the output voltage amplitude.

The voltage control loop can be designed as follows:

$$\begin{cases} i_{1dref} = -\omega C_f u_q + (K_{\mathrm{p1}} + K_{\mathrm{i1}}/s)(u_{d\mathrm{ref}} - u_d) + i_d \\ i_{1qref} = \omega C_f u_d + (K_{\mathrm{p1}} + K_{i1}/s)(u_{q\mathrm{ref}} - u_q) + i_{\mathrm{q}} \end{cases} \tag{A6}$$

where i_{1dref} and i_{1qref} are the reference current commands for the d-axis and q-axis, respectively, in the synchronous rotating coordinate system; i_d and i_q are the currents at the PCC points for the d-axis and q-axis, respectively, in the synchronous rotating coordinate system; u_{dref} and u_{qref} are the reference voltages at the PCC points on the d-axis and q-axis, respectively, in the synchronous rotating coordinate system; u_d and u_q are the voltages at the PCC points on the d-axis and q-axis, respectively, in the synchronous rotating coordinate system; K_{p1} and K_{i1} are the proportional and integral coefficients of the PI control.

The current control loop can be designed as follows:

$$\begin{cases} e_{dref} = -\omega L_f i_{1q} + (K_{\mathrm{p2}} + K_{\mathrm{i2}}/s)(i_{1d\mathrm{ref}} - i_{1d}) + u_d \\ e_{qref} = \omega L_f i_{1d} + (K_{\mathrm{p2}} + K_{i2}/s)(i_{1q\mathrm{ref}} - i_{1q}) + u_q \end{cases} \tag{A7}$$

where e_{dref} and e_{qref} are the modulation voltages for the d-axis and q-axis, respectively, in the synchronously rotating coordinate system; i_{1d} and i_{1q} are the current commands for the d-axis and q-axis, respectively, in the synchronously rotating coordinate system; K_{p2} and K_{i2} are the proportional and integral coefficients of the PI control.

References

1. Ma, N.; Xie, X.; Dong, W.; Li, H. Wideband Dynamic Monitoring and Control System for Power Systems with High Penetration of Renewable Energy and Power Electronics. *Sustainability* **2025**, *17*, 8334. [CrossRef]
2. Yang, Y.; Wen, Y.; Zhang, Z.; Dong, Y.; Shen, C.; Liu, Y. Toward 100% Renewable Power Grids: A Review. *IEEE Access* **2025**, *13*, 69690–69704. [CrossRef]
3. Liu, R.; Xiao, H.; Wu, Z.; Shi, J.; Wang, B.; Xiao, H.; Hu, D.; Jia, Z.; Zhao, G.; Li, Y. Small-Signal Stability of Large-Scale Integrated Hydro–Wind–Photovoltaic Storage (HWPS) Systems Based on the Linear Time-Periodic (LTP) Method. *Processes* **2025**, *13*, 3500. [CrossRef]
4. Liu, N.; Wang, H.; Zhou, D.; Shi, H.; Chen, Z. Comprehensive review of power system oscillations in large-scale power electronic-based renewable energy power plants. *J. Renew. Sustain. Energy* **2023**, *15*, 042701. [CrossRef]
5. Krein, P.T.; Bentsman, J.; Bass, R.M.; Lesieutre, B.L. On the use of averaging for the analysis of power electronic systems. *IEEE Trans. Power Electron.* **1990**, *5*, 182–190. [CrossRef]
6. Chen, X.; Wang, Y.; Gong, C.; Sun, J.; He, G.; Li, G.; Wang, H. Overview of Stability Research for Grid-Connected Inverters Based on Impedance Analysis Method. *Proc. CSEE* **2018**, *38*, 2082–2094. [CrossRef]
7. He, Y.; Zhou, B.; Li, Y.; Peng, F.Z. Impedance Modeling and Stability Analysis for the PLL-less and Voltage Sensor-less Grid-tied Converters. In *2023 IEEE 17th International Conference on Compatibility, Power Electronics and Power Engineering (CPE-POWERENG)*; IEEE: Piscataway, NJ, USA, 2023; pp. 1–5. [CrossRef]
8. Han, F.; Zhang, X.; Li, M.; Li, F.; Zhao, W. Stability Control for Grid-Connected Inverters Based on Hybrid-Mode of Grid-Following and Grid-Forming. *IEEE Trans. Ind. Electron.* **2024**, *71*, 10750–10760. [CrossRef]
9. Wang, L.; Liang, J.; Zeng, S.; Fan, H.; Li, L.-B.; Kang, W. Research on power decoupling of parallel virtual synchronous machine based on feedforward control. In *2021 IEEE 4th International Electrical and Energy Conference (CIBEC)*; IEEE: Piscataway, NJ, USA, 2021; pp. 1–5. [CrossRef]
10. Wu, W.; Chen, Y.; Zhou, L.; Luo, A.; Zhou, X.; He, Z. Sequence Impedance Modeling and Stability Comparative Analysis of Voltage-Controlled VSGs and Current-Controlled VSGs. *IEEE Trans. Ind. Electron.* **2019**, *66*, 6460–6472. [CrossRef]
11. Wu, W.; Zhou, L.; Chen, Y.; Luo, A.; Dong, Y.; Zhou, X. Sequence-Impedance-Based Stability Comparison Between VSGs and Traditional Grid-Connected Inverters. *IEEE Trans. Power Electron.* **2019**, *34*, 46–52. [CrossRef]
12. Hidalgo Monsivais, L.C.; León Ruiz, Y.; Hernández Ramírez, J.C.; Visairo-Cruz, N.; Segundo-Ramírez, J.; Barocio, E. Controller Hardware-in-the-Loop Validation of a DSP-Controlled Grid-Tied Inverter Using Impedance and Time-Domain Approaches. *Electricity* **2025**, *6*, 52. [CrossRef]
13. Yuan, J.; Ma, M.; Jia, Y. Transient Stability Analysis for the Wind Power Grid-Connected System: A Manifold Topology Perspective on the Global Stability Domain. *Electricity* **2025**, *6*, 44. [CrossRef]

14. Ullah, A.; Ullah, S.; Hussan, U.; Zheng, D.; Bao, D.; Pan, X. Maximum Power Extraction from a PMSG-Based Standalone WECS via Neuro-Adaptive Fuzzy Fractional Order Super-Twisting Sliding Mode Control Approach with High Gain Differentiator. *Fractal Fract.* **2026**, *10*, 158. [CrossRef]
15. Zhang, X.; Xie, Y.; Wu, R. A Capacitor-Current-Feedback Active Damping Control Strategy With Phase Lead Compensation for LCL-Type Grid-Connected Inverter. *IEEE Access* **2024**, *12*, 193663–193675. [CrossRef]
16. Zhang, L.; Qin, A.; Qian, Q.; Zobaa, A.F.; Abdelkader, S.M.; Mansour, D.-E.A. Inverter-Side Current Feedback Active Damping Based on Phase-Lead Compensation for Grid-Connected Inverter. In *2025 IEEE Conference on Power Electronics and Renewable Energy (CPERE)*; IEEE: Piscataway, NJ, USA, 2025; pp. 1–7. [CrossRef]
17. Khalfalla, H.; Ethni, S.; Kadandani, N.B.; Pickert, V. Resonance Frequency Detection Technique in Gridconnected Inverter Systems Based on Double-order Digitalized Filter. In *2019 10th International Renewable Energy Congress (IREC)*; IEEE: Piscataway, NJ, USA, 2019; pp. 1–6. [CrossRef]
18. Yang, H.; Sun, Z.; Wang, H.; Wang, Y.; Zhu, M.; Guo, L.; Zhou, G.; Lyu, H. Adaptive Virtual Impedance Droop Control of Parallel Inverters for Islanded Microgrids. *Sensors* **2025**, *25*, 5166. [CrossRef] [PubMed]
19. Zhang, J.; Zhang, T. Research on the Circulating-Current Suppression of Parallel Inverters Based on Droop Control. In *2018 IEEE International Conference on Mechatronics and Automation (ICMA)*; IEEE: Piscataway, NJ, USA, 2018; pp. 2260–2264. [CrossRef]
20. Yang, D.; Ruan, X.; Wu, H. A Real-Time Computation Method With Dual Sampling Mode to Improve the Current Control Performance of the LCL-Type Grid-Connected Inverter. *IEEE Trans. Ind. Electron.* **2015**, *62*, 4563–4572. [CrossRef]

Disclaimer/Publisher's Note: The statements, opinions and data contained in all publications are solely those of the individual author(s) and contributor(s) and not of MDPI and/or the editor(s). MDPI and/or the editor(s) disclaim responsibility for any injury to people or property resulting from any ideas, methods, instructions or products referred to in the content.